

In Situ Process Monitoring and Multichannel Imaging for Vacuum-Assisted Growth Control of Inkjet-Printed and Blade-Coated Perovskite Thin-Films

Fabian Schackmar,* Felix Laufer, Roja Singh, Ahmed Farag, Helge Eggers, Saba Gharibzadeh, Bahram Abdollahi Nejand, Uli Lemmer, Gerardo Hernandez-Sosa, and Ulrich W. Paetzold*

Vacuum-assisted growth (VAG) control is one of the most promising methods for controlling nucleation and crystallization of printed and coated large area lead halide perovskite-based layers for optoelectronics. To coat or print homogeneous high-quality perovskite thin-films at high fabrication yield, real-time process monitoring of the VAG is pivotal. In response, a 2.1-megapixel multi-channel photoluminescence (PL) and reflection imaging system is developed and employed for the simultaneous spatial in situ analysis of drying, nucleation, and crystal growth during VAG and subsequent thermal annealing of inkjet-printed and blade-coated perovskite thin-films. It is shown that the VAG process, for example, evacuation rate and time, affects the film formation and provide detailed insight into traced PL and reflection transients extracted from sub-second videos of each channel. Based on correlative analysis between the transients and, for example, perovskite ink composition, wet-film thickness, or evacuation time, key regions which influence crystal quality, film morphology, and are base for prediction of solar cell performance are identified.

1. Introduction

The research and progress of metal halide perovskite-based optoelectronics over the last decade led to highly efficient

F. Schackmar, F. Laufer, R. Singh, H. Eggers, U. Lemmer, G. Hernandez-Sosa, U. W. Paetzold
Karlsruhe Institute of Technology (KIT)
Light Technology Institute (LTI)
Engesserstrasse 13, 76131 Karlsruhe, Germany
E-mail: fabian.schackmar@kit.edu; ulrich.paetzold@kit.edu

F. Schackmar, H. Eggers, U. Lemmer, G. Hernandez-Sosa
InnovationLab

Speyerer Strasse 4, 69115 Heidelberg, Germany

F. Schackmar, R. Singh, A. Farag, H. Eggers, S. Gharibzadeh, B. Abdollahi Nejand, U. Lemmer, G. Hernandez-Sosa, U. W. Paetzold
Karlsruhe Institute of Technology (KIT)
Institute of Microstructure Technology (IMT)
Hermann-von-Helmholtz-Platz 1, 76344 Eggenstein-Leopoldshafen, Germany

 The ORCID identification number(s) for the author(s) of this article can be found under <https://doi.org/10.1002/admt.202201331>.

© 2022 The Authors. Advanced Materials Technologies published by Wiley-VCH GmbH. This is an open access article under the terms of the Creative Commons Attribution-NonCommercial License, which permits use, distribution and reproduction in any medium, provided the original work is properly cited and is not used for commercial purposes.

DOI: 10.1002/admt.202201331

laboratory-scale solar cells, photo- and X-ray detectors,^[1–3] and light emitting diodes.^[4] Meanwhile, perovskite solar cells exceed 25% power conversion efficiency (PCE) in single junction^[5] and surpassed 30% in monolithic silicon-perovskite-tandem solar cells.^[6] This shifts the research focus to the development of scalable manufacturing methods for high-throughput production lines and large area deposition techniques. While the two established competing approaches, thermal evaporation and solution-based deposition, are fundamentally different, monitoring both processes in real-time is of utmost importance to ensure a constant high-quality crystallization throughout the complete fabrication process. The perovskite crystal growth in both techniques is for example impacted by the choice of

substrate and thereby the corresponding surface free energy and roughness,^[7,8] highlighting the need to control crucial process-specific parameters. For solution-based deposition techniques, the drying of a deposited perovskite precursor containing wet-film and the subsequent nucleation is one of the most critical process steps. Established procedures for initialization and control of this nucleation step are antisolvent quenching,^[9,10] convective or radiative thermal treatment,^[11,12] laminar or perpendicular gas flow quenching,^[13,14] and vacuum-assisted growth (VAG) control.^[15–17] Antisolvent quenching is the method of choice in spin-coated high efficiency, small-area devices and was transferred to up-scalable varieties like spraying and bathing, but requires large amounts of mostly harmful solvents.^[10,18] Thermal treatment without aid of one of the other methods is mostly used for CH₃NH₃PbI₃-(MAPI)-based perovskites which do not meet the stability requirements for commercialization.^[19,20] While gas flow quenching is widespread in coating applications like slot-die and blade coating making it ideal for in-line and role to role production,^[21] VAG is a preferred route for controlling the morphology of inkjet-printed perovskite thin films in batch processing.^[22] Unlike gas flow quenching or antisolvent quenching, VAG does not impact the shape of the printed wet-film pattern, thereby maintaining a key advantage of digital printing. In contrast, the required high gas flow rates^[14] used for conventional gas flow quenching, result in a flow of the ink in wet-film, which deforms printed

digital patterns. This is particularly pronounced if high boiling point solvents are used in the ink as in most publications on inkjet-printed perovskites.^[22] Next to high-quality perovskite thin-films that achieve stabilized power conversion efficiencies up to $\approx 18.5\%$ for inkjet printing combined with VAG,^[23] VAG was also employed for other coating techniques such as spray coating,^[24] slot-die coating,^[25] blade coating,^[26] and evolves as method for spin-coated planar, large-area ($>26\text{ cm}^2$) modules,^[15] perovskite tandem devices,^[27,17,28] and Sn-based perovskite photovoltaics.^[17,29–31]

In the following, the VAG process stages are revisited: First, it should be noted that the VAG process is independent of the wet-film deposition technique. Subsequent to the deposition step, the perovskite precursor containing wet-film of certain thickness is to be placed in a vacuum chamber. The subsequent VAG process can be described as in ref. [32] after LaMer and Dinegar, where the evaporation of the solvent(s) leads to an increasing precursor concentration, until a critical concentration in the supersaturated solution is reached and rapid self-nucleation is induced, followed by crystal growth. The optimum VAG process conditions depend on a variety of parameters such as the solvent evaporation rate which in turn relates to the pump rate, chamber dimensions, utilized solvents, and evacuation time. In order to understand the thin-film formation of polycrystalline perovskite thin-films and the interplay with the aforementioned process parameters, it is necessary to monitor VAG in situ. In situ characterization techniques based on electron^[33,34] and X-ray^[35–39] probes give crucial insights into evolving crystal structures and compositions but are difficult to realize in production lines. In contrast, optical characterization techniques based on photons in the wavelengths range from UV to near infrared have been applied in production so far, for example photoluminescence (PL) imaging in Si- and CuInGaSe₂-photovoltaics,^[40,41] and can be operated in ambient environments. Common characterization techniques used for perovskites so far encompass Raman spectroscopy,^[42,43] thermography,^[44] absorption and reflection spectroscopy,^[45–48] and PL spectroscopy.^[45,49] In contrast to Raman spectroscopy, which is limited to small monitoring areas due to the need of a focused laser beams, PL can be used as a large area imaging method. While spectrally resolved in situ PL (in combination with a light microscope) of inkjet-printed Cs_{0.05}(FA_{0.83}MA_{0.17})_{0.95}Pb(I_{0.83}Br_{0.17})₃ (C₅-TCP) perovskites during VAG was demonstrated before,^[50] spatial information as provided by camera images is needed to obtain information of the entire film. Spatial monitoring of drying thin-films in real-time including PL microscopy can be used to observe edge-regions and detect inhomogeneities or defects^[51] in the active area not visible by eye (or conventional light microscopy).^[52]

In response, we demonstrate here an in situ PL and reflection imaging setup to monitor layer formation of solution-processed, that is, inkjet-printed and blade-coated, thin-films of different perovskite compositions during VAG and subsequent thermal annealing. For this purpose, we modified a four-channel in situ imaging system first introduced by Ternes et al.^[51] (see Figure S1, Supporting Information), which was used to detect defects in blade-coated MAPI layers dried in a laminar gas flow. The four imaging channels include one reflection and three filtered PL channels, of which the PL

intensity and PL peak wavelength is extracted. We show the formation of common non-Cs-containing perovskite compositions like MAPI or CH(NH₃)₂PbI₃ (formamidinium lead triiodide, FAPI) as well as state-of-the-art compositions like Cs_{0.1}(FA_{0.83}MA_{0.17})_{0.9}Pb(I_{0.85}Br_{0.15})₃ (triple cation perovskite, C₁₀-TCP) and Cs_{0.17}FA_{0.83}Pb(I_{0.91}Br_{0.09})₃ (double cation perovskite, DCP). On the example of DCP, we demonstrate the influence of the substrate surface, ink composition and VAG process parameters on the PL and reflection signals. Moreover, we correlate them to morphology changes and photovoltaic performance with the aim to prescreen devices and create a guide for automated process control and performance prediction, which could potentially be transferred to alternative drying techniques.

2. Spatial In Situ Monitoring of Vacuum-Assisted Drying and Annealing

The VAG process consists of four basic process stages during the perovskite thin-film formation (i–iv). They are shown along with the in situ setup in **Figure 1a** and explained in detail in the following. Wet-films of perovskite precursor ink are prepared via inkjet printing and blade coating and placed in the vacuum chamber. The VAG process starts with the drying (phase I) of the wet film, followed by the phase of nucleation and crystal growth (phase II) as explained by LaMer and Dinegar:^[32] i) With the start of the evacuation the pressure approaches the vapor pressure of the solvent(s), which results in vastly enhanced solvent evaporation rate(s), accelerating the drying process (phase I), and increasing the concentration of the precursor salts inside the thinning wet-film. ii) As the vacuum is maintained, the solution reaches the state of supersaturation, a critical concentration is reached, and rapid self-nucleation of the perovskite crystallites is initiated, followed by a diffusion-driven crystal growth (phase II). iii) After the crystal formation, the chamber is vented to the base atmosphere again and iv) a final thermal annealing step is applied.

We monitor the perovskite film formation during VAG by illumination (two blue LED arrays) of the film through the transparent acrylic glass lid of the vacuum chamber and detection of the signals with a monochrome scientific CMOS (sCMOS) camera. The reflected light and the PL emitted from the perovskite film (if any) are recorded through four different optical filters mounted on a spinning wheel, producing four different parallel image acquiring channels: a neutral density (ND) filter to monitor the light reflected from the surface (including contributions from the background underneath the substrate), a 725 nm cut-on wavelength (WL) longpass (LP725), a 780 nm cut-on WL longpass (LP780), and 775 nm cut-off WL shortpass (SP775, together with a 665 nm longpass to exclude any excitation light. For further setup details see Supporting Information). The spectral filters are chosen with regard to an optical bandgap of $\approx 1.59\text{ eV}$. As such, the SP775 channel signal includes the low WL half of the spectrum, the LP780 the higher WL part, and the LP725 includes the complete Gaussian PL emission (compare transmittance spectra of the filters in Figure S1c,d, Supporting Information). The LP725 channel can therefore be used as a measure for the PL intensity. In addition, the pressure of each VAG process

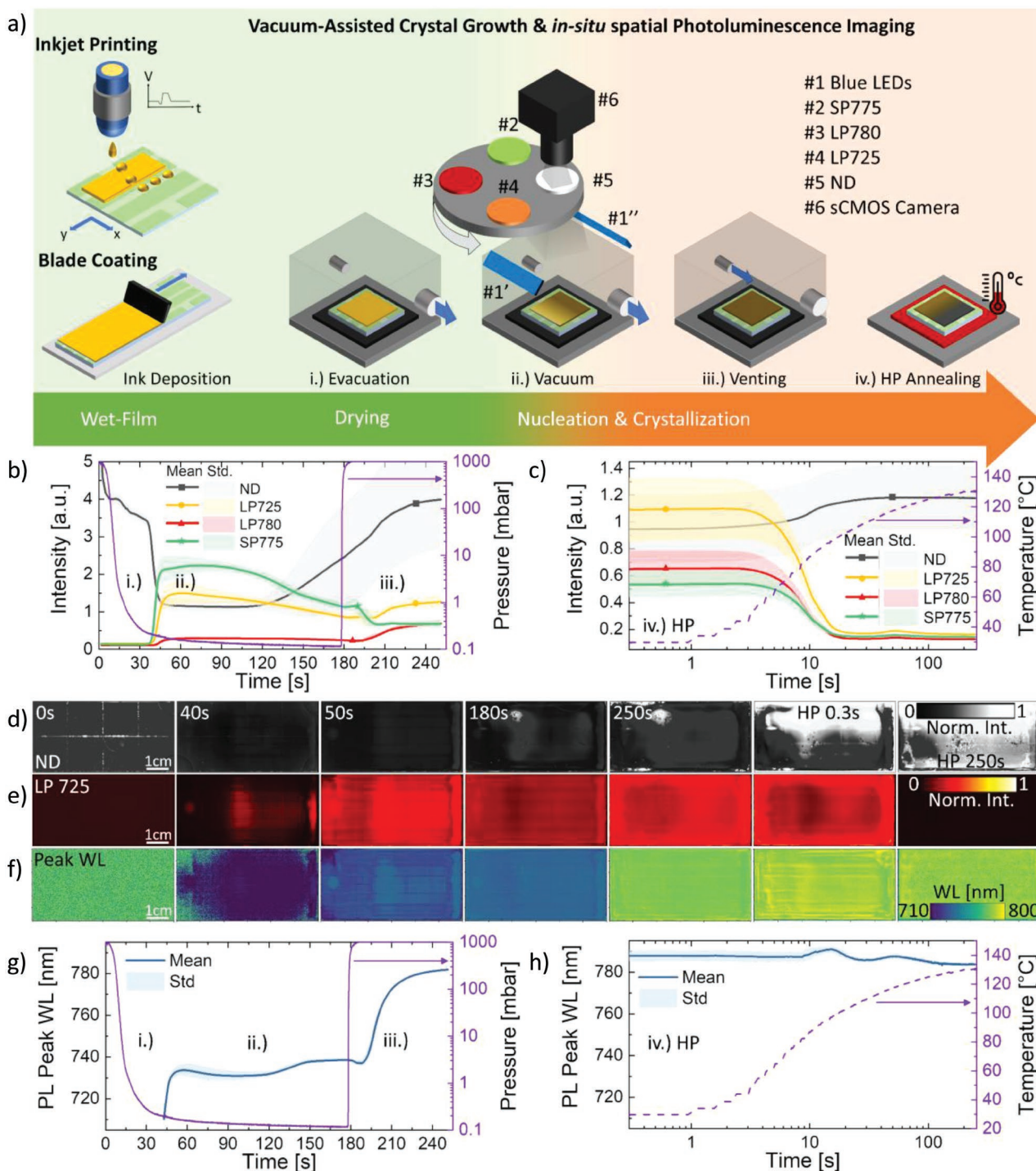


Figure 1. a) Schematic of the setup, covering spatially resolved *in-situ* photoluminescence (PL), and key steps in vacuum-assisted crystal growth (VAG) of a perovskite wet-film after deposition by inkjet printing or blade coating: two blue LED bars (#1' & #1'') illuminating the sample surface excite a forming perovskite thin-film; the reflection from the surface and emitted PL is filtered through four optical filters (#2–5) mounted on a rotating wheel and captured by an sCMOS camera (#6); these four image channels observe VAG, which is dividable in sole drying while i) initial chamber evacuation and subsequently enhanced solvent evaporation rate, ii) applied vacuum and the start of nucleation and crystal growth, iii) venting of the chamber, and iv) a final hotplate (HP) annealing step. Exemplary time-resolved intensity signals of each channel during VAG of a blade-coated $\text{Cs}_{0.17}\text{FA}_{0.83}\text{PbI}_{2.73}\text{Br}_{0.27}$ (DCP) thin-film b) inside the vacuum chamber shown together with the monitored process pressure and c) on an HP with corresponding substrate temperature. The mean intensity and standard deviation (Std.) of the channel signals are calculated from central areas of each frame, shown for characteristic times for d) the ND-channel exhibiting the surface reflection, for e) the LP725-channel displaying the PL intensity and for f) the PL peak wavelength (WL) extracted from channels #2–4. Corresponding time-resolved PL peak WL g) inside the vacuum chamber and h) while HP annealing. The ND signal intensity is reduced by a factor 5 in (a) and 20 in (b) for comparison.

is tracked and the substrate temperature is monitored during hotplate (HP) annealing. Altogether, the spatially resolved in situ monitoring system provides for each VAG process a data set of four 2.1-megapixel image channels over ≈ 250 s with a 0.3 s temporal resolution as well as the corresponding pressure (temperature) evolution. Each dataset can be presented as a transient of the four image channels and the pressure, which is condensed to the mean values of the spatial information in the central region as demonstrated exemplarily in Figure 1b for VAG and Figure 1c for the consecutive HP annealing for the drying of a DCP thin-film. The DCP film is blade-coated on the following substrate glass/indium tin oxide (ITO)/NiO_x/2PACz (2-(9H-carbazol-9-yl)ethyl]phosphonic acid)). The image and therefore the original spatial information are provided at characteristic times for the ND channel in Figure 1d and the LP725 channel in Figure 1e.

The four stages of the perovskite thin-film formation during the VAG process are apparent in the transients of Figure 1b,c: i) First, the drying stage ($t \approx 0$ s to ≈ 35 s), where the pressure in the chamber rapidly decreases and the solvents (ternary system consisting of *N,N*-dimethylformamide (DMF), dimethyl sulfoxide (DMSO), and γ -butyrolactone (GBL)) evaporate, thinning the wet-film (phase I). The change in wet-film thickness is apparent by the change in reflection in the ND channel. In this stage, the PL channels exhibit only a constant noise signal, since there is no PL emitted yet. ii) Second, phase II starts with the occurring nucleation and crystallization ($t \approx 35$ s to ≈ 180 s). The appearance of the perovskite layer changes to the expected brownish visual color and the ND/reflection drops significantly along with the PL on-set seen in the signal intensity rise in all PL channels LP725, LP780, and SP775. It should be noted that the intensity of the filtered PL channels is shown relative to each other, while the ND intensity is not correlated. iii) The third phase starts with the venting of the chamber ($t \approx 180$ s till end), which takes around 25–30 s to reach the ambient atmosphere again. In this stage, the ND/reflection and LP725/PL signal increases. The PL is red-shifted, as it can be seen from the LP780 intensity increase and SP775 decrease (reasons for the shapes will be discussed in detail below). Finally, the substrate is placed for stage (iv), the thermal annealing, on an HP (see Figure 1c). As the substrate temperature rises, the PL channels decline after ≈ 3 s (at ≈ 50 °C) toward noise level till there is only a low signal detectable after ≈ 100 °C. This is supposedly a result of complete conversion of the perovskite by the removal of the last solvent residuals paving the way for fast transport processes of the excited charge carriers to the hole transport layer (HTL) and ITO^[49,53] and thermally induced PL quenching through higher non-radiative recombination at elevated temperature.^[54,55] Simultaneously, the ND/reflection increases as the PL drops (till ≈ 11 s) after the start of thermal annealing (appearance change is visible by eye), indicating a change in morphology, possibly due the solvent extraction and complete conversion changing the absorption profile.^[49]

From the acquired spatial and time-resolved data set, we can derive the PL peak WL after a model introduced by Chen et al.^[56] (details in Experimental Section). Figure 1f depicts the PL peak WL at each pixel at the same characteristic times than reflectance and PL intensity and Figures 1g and 1h show the transient evolution of the same central areas in the vacuum

chamber and on the hotplate, respectively. The VAG stages introduced above are apparent again: i) While there is no PL in the drying stage, ii) the second stage starts with a fast red-shift from ≈ 710 nm to ≈ 735 nm indicating nucleation and fast growth of the seed crystals. iii) The PL peak WL remains unchanged until the venting with air leads to a strong red-shift till the final nominal PL peak WL of ≈ 780 nm. iv) On the hotplate, the PL peak WL shows little variation, indicating no major change in chemical composition of the crystals or surface morphology. It should be noted that the PL peak WL offset between Figure 1g,h might arise from the different background correction used for hotplate monitoring (see Experimental Section).

In addition to the PL peak WL data, the full spectrally resolved PL signal is monitored on a single spot with a fiber inside the vacuum chamber. The mean value extracted of the image channels of the spot where the spectrometer's fiber is aligned in comparison to the PL peak WL of the spectrometer are in good agreement (see Figure S2, Supporting Information) and the assumption the PL peak WL can be acquired spatially throughout the whole crystallization we see as justified.

It is highlighted that the VAG monitoring process is suitable to study a wide range of perovskite compositions, given certain conditions are met. For similar compositions like Cs_{0.1}FA_{0.75}MA_{0.15}Pb(I_{0.85}Br_{0.15})₃ (C₁₀-TCP) or CsCl_{0.17}FA_{0.83}PbI₃, with slight variations in bandgap due to different halogen incorporation, and different choice of precursor salts, the formation of the perovskite seems to be comparable (see Figures S3 and S4, Supporting Information). However, for Cs-poor Pb-based compositions, the thin-film formation does not occur in full during VAG alone. While the change from (i) to (ii) is observed, the PL signal remains weak and the thin-film color stays yellow. The formation does not arise until heat is applied, for example, demonstrated for FAPb(I_{0.91}Br_{0.09})₃ on a hotplate after VAG (see Figure S5, Supporting Information) or for MAI:PbI₂ during VAG (Figure S6, Supporting Information). Pb-based compositions with Cs < 3%, here MA-free Cs_{0.17}FA_{1-0.83}Pb(I_{0.91}Br_{0.09})₃, show a different crystallization behavior (compare Figure S7, Supporting Information), in agreement with ref. [57] (shown for Cs_{0.01}(FA_{0.85}MA_{0.15})_{1-0.9}Pb(I_{0.85}Br_{0.15})₃). Therefore, multi-channel imaging for VAG requires either Pb-based perovskite compositions with a minimum Cs amount $\geq 3\%$ or thermal treatment while under vacuum and the spectral filter set needs to be adapted to the bandgap of the composition. It should be mentioned that Sn-based and Sn:Pb-mixed perovskites form during VAG also for Cs-free compositions.^[17]

3. Monitoring the VAG Process Phases

Figure 1 provides an overview of a complete captured data set. In the following, we study the interrelation between key process parameters and the phase transition of a wet-film to a polycrystalline thin-film by spatially-resolved in situ monitoring of the four VAG process stages. As a representative and state-of-the-art perovskite composition and corresponding ink, we use a DCP solution based on the solvents DMF, DMSO, and GBL (8:2:5 vol:vol:vol) for inkjet printing and for blade coating. The former represents a deposition technique that allows for a precise control of the deposited ink volume (and thereby

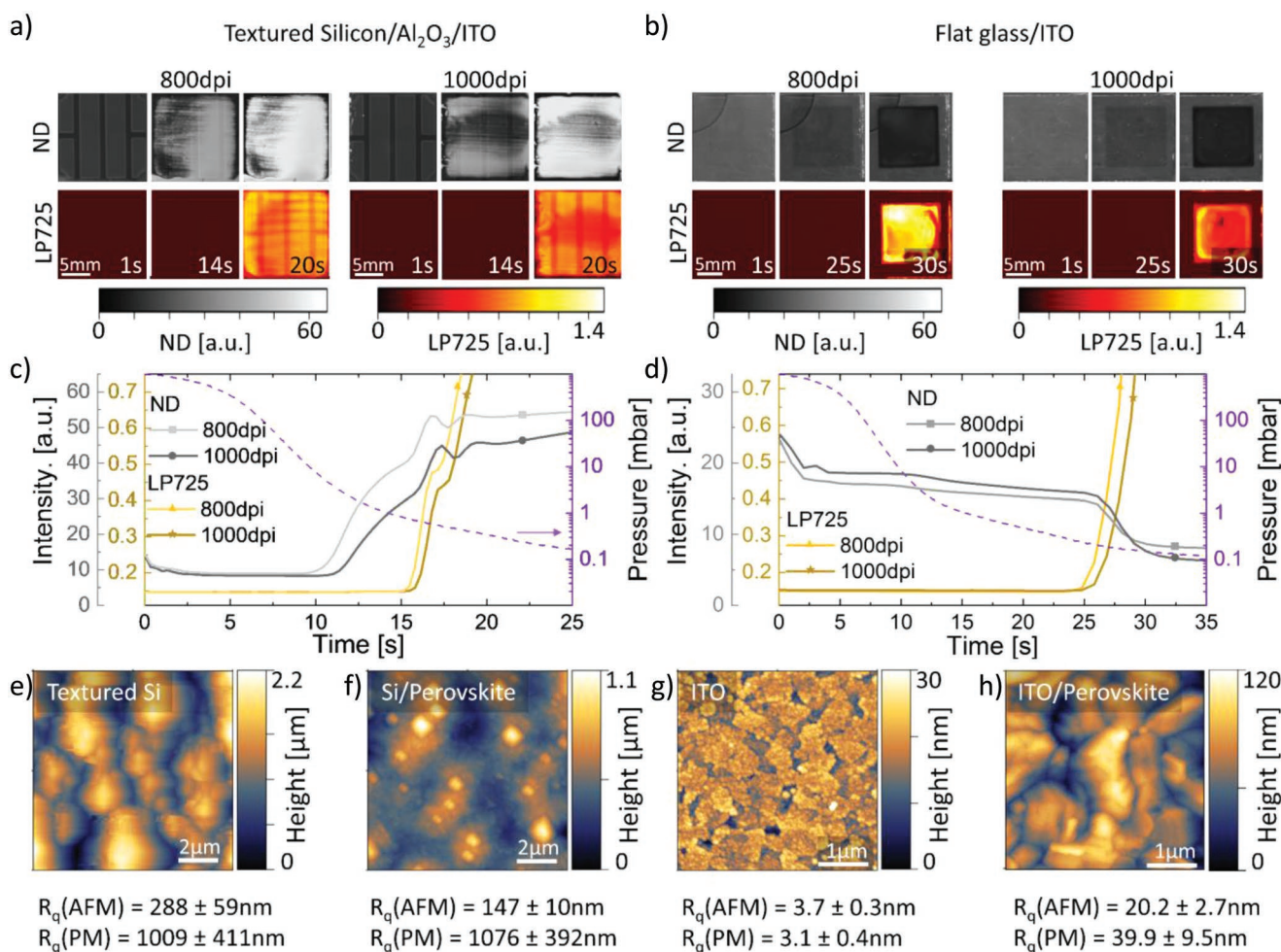


Figure 2. Phase I Drying: ND- and LP725-channel image cut-outs of inkjet-printed DCP squares with 800 dpi and 1000 dpi resolution on a) textured Si substrates and b) flat glass/ITO substrates at characteristic times. Transient intensity of the central $8.5 \times 8.5 \text{ mm}^2$ square area of the ND- and LP725-channel of the same c) textured Si and d) glass/ITO substrates. Atomic force microscopy (AFM) surface profiles and extracted RMS roughness R_q from AFM and profilometer (PM) measurements (along $\approx 1 \text{ mm}$) of the bare substrate and the annealed perovskite layer on top after completion: e) Si, f) DCP on Si, g) ITO, and h) DCP on ITO. It should be noted that the total solvent volume (number of samples) in the vacuum chamber is different in both experiments, hence the PL on-set delay ($\approx 5.0 \mu\text{L}$ and $\approx 17.2 \mu\text{L}$).

wet-film thickness) and the latter represents a technique for rapid large-area wet-film application.

3.1. Phase I: Drying

Phase I, drying, starts immediately once the wet-film is placed in a vacuum chamber and the process stage (i), the evacuation, is initiated. The pressure quickly drops, approaching and finally exceeding the vapor pressures of the ink's solvents DMF, DMSO, and GBL (see Figure S8, Supporting Information, showing vapor pressures at 20°C , approximately the chamber's initial temperature) and thus increasing the evaporation rate. In this phase, the wet-film thickness is decreasing rapidly, as it can be estimated by the calculated wet-film thickness $t_{\text{wet-film}}$ and the measured final dry-film thickness $t_{\text{dry-film}}$ (see Table S1, Supporting Information, for resolutions and corresponding wet-film thicknesses). Since there is no PL emitted, only the ND/reflection channel is observed.

The ND channel is used to identify significant changes in (diffuse) reflection caused by changing surface roughness or increased absorption. By using textured substrates with peak-to-valley roughness $R_z \gg t_{\text{dry-film}}$, the influence of a rough surface on the reflection signal during the drying phase is discussed. The found correlations of the monitoring system can be utilized to analyze process-related origins of rough surfaces as will be discussed below (and it can be seen in Figures S5 and S6, Supporting Information, for MAPI and FAPI, where the flat wet-film becomes a rougher low absorbing visually yellow appearing film). To test this hypothesis, we use textured Si with R_z of $\approx 2\text{--}3 \mu\text{m}$, which will be covered by a flat inkjet-printed wet-film (greater than $\approx 10 \mu\text{m}$) and the roughness should appear while drying (final dry-film thickness on a flat glass substrate $< 1 \mu\text{m}$). The reflection and PL intensity images of inkjet-printed (IJP) DCP wet-films of two resolutions are shown for characteristic times in Figure 2a on textured Si and Figure 2b on flat glass/ITO. Additionally, the transient evolution of the central area of the thin-films shown from

phase (i) drying till phase (ii) nucleation and crystallization is depicted in Figure 2c,d. By comparing both substrate types, the difference is apparent: for both wet-film thicknesses, the ND signal rises seconds before the PL signal starts and stays high after the PL on-set in case of the textured substrate. Whereas for the flat glass/ITO substrate the ND signal declines at the time of the PL on-set and remains at a low level afterward. This trend is attributed to the initially larger thickness of the wet-film ($t_{\text{wet-film}}$) compared to the roughness (R_z) of the textured Si-substrate, resulting in an overall planar wet-film surface with low light scattering (compare schematic in Figure S9, Supporting Information). During the drying phase, the volume of the wet-film reduces and consequently, at some point, the pyramid peaks (shown by atomic force microscopy (AFM) images in Figure 2e) appear, introducing a noticeable roughness. The incident light is scattered at the rough surface, increasing the normal reflection, that is, the intensity measured by the camera. Figure 2f depicts pyramid peaks at the film surface of the dry-film along with an increased root mean square (RMS) roughness R_q extracted microscopically from AFM measurements and macroscopically from a profilometer (PM). In contrast, for the flat substrate (see Figure 2g), the wet-film thickness monotonously decreases during the drying phase. Once the perovskite thin-film is formed, the absorption increases (see Figure 2h). The thinner wet-film (printed with 800 dpi) reaches the dry-film state earlier compared to the wet film printed with 1000 dpi film. For the rough substrate, the reflection increases and the absorption dip for the flat ITO substrate starts earlier. It should be noted that the ND channel represents the reflection normal to the surface weighted with the emission spectrum of the LEDs, the transmittance of the lenses, and the spectral response of the camera. The reflectance normal to the surface increases with a higher ratio of the diffuse reflectance compared to the specular reflectance (see Figure S10, Supporting Information).

In summary, significant changes in roughness can be identified by using the ND channel. While up to now the substrate surface roughness was distinguished, it is shown below that roughness changes caused by the crystallization of the perovskite thin-film are detected as well.

3.2. Phase I to Phase II: Start of Nucleation and Crystal Growth of the Perovskite Thin-Film

The drying phase ends once the precursor concentration in the wet-film exceeds a critical point and nucleation occurs to relieve the supersaturation state. As soon as the nucleation of the perovskite crystallites begins, the PL emission below the bandgap of the perovskite thin film appears. The PL on-set time is a characteristic parameter, since it correlates to important thin-film characteristics and can be used for process control, as discussed below.

The on-set of the nucleation and therefore the PL on-set time depends on the evaporation rate of the ink's solvents, the wet-film thickness, the precursor materials concentration as well as their solubility. Furthermore, the evaporation rate depends on the ink and the solvent system, particularly their vapor pressures, and the evacuation rate of the vacuum chamber. As the

evaporation rate and the ink system are invariant in established processes, we first discuss these process parameters.

3.2.1. Nucleation On-Set: Ink and Evacuation Rate

The solvent system of the ink affects the homogeneity of the dried thin-film and drying rate and therefore the nucleation on-set. Key characteristics are the boiling point, vapor pressure, surface tension (SFT), and viscosity. It should be noted that all these parameters are temperature and/or pressure dependent and that solvent ion/molecule interactions predefine intermediate phases in the solution therefore influencing the crystallization.^[58–60] The most common solvents for perovskite solutions are of the polar aprotic group, although others are used as well.^[61–63] For IJP perovskite thin-films, a mixture of DMF, DMSO, and GBL is widely established.^[22] DMF has the highest vapor pressure, followed by GBL and DMSO (see Figure S8, Supporting Information). The influence of the solvent system DMF:DMSO(:GBL) on the PL on-set is shown in Figure S11, Supporting Information: A blade-coated DCP precursor system dissolved in pure DMF crystallizes ≈ 5 times faster compared to pure DMSO (see Figure S11a,b, Supporting Information), since the chamber pressure reaches the vapor pressure of DMF much earlier, resulting in a higher evaporation rate of DMF. A single solvent system and mixtures of these two solvents lead to inhomogeneous dried films, wherefore the PL on-set times are deduced from linear fits of the resulting (inhomogeneous) dry-films to rule out a wet-film thickness effect (see Figure S11c,d, Supporting Information). The relative evaporation rate of the solvent systems is apparent in the slope of the PL on-set time plotted over film thickness and emphasized through linear fits. The influence of the solvents is additionally monitored in the vacuum pressure during VAG compared to the pressure transient of an empty chamber: the evaporation of pure DMSO film leads to a pressure increase in the chamber (i.e., a DMSO solvent vapor atmosphere), while the volatile DMF is immediately evacuated (see Figure S9b,a, Supporting Information).

Moreover, the choice of solvents influences the solubility of the precursor salts and intermediate phases in the solution and in not (yet) fully annealed thin-films.^[59] For iodine-rich lead-based perovskite, the solubility of the solvents is in the order DMF > DMSO \gg GBL^[63–66] and the coordination ability of Pb^{2+} DMSO > DMF \gg GBL.^[66] Higher solute concentration (or lower solubility) of a precursor salt in the solution would lead to an earlier PL on-set, since the wet-film will reach the solubility limit and the oversaturation state earlier.

Finally, the evacuation rate is investigated and varied which is expressed in the pressure evolution in the vacuum chamber. Figure 3a shows the process pressure for four different evacuation rates during VAG of a blade-coated DCP film and the corresponding times when the level of 0.5 mbar is reached. Compared to the pressure evolution of an empty chamber, the process pressure evolution during VAG decays slower and hence shows an apparent solvent atmosphere. This solvent atmosphere is more pronounced for slower evacuation rates, as shown in Figure S12, Supporting Information.

A lower evacuation rate results in a slower drying and thus, the nucleation occurs later as indicated by the shift in PL on-set

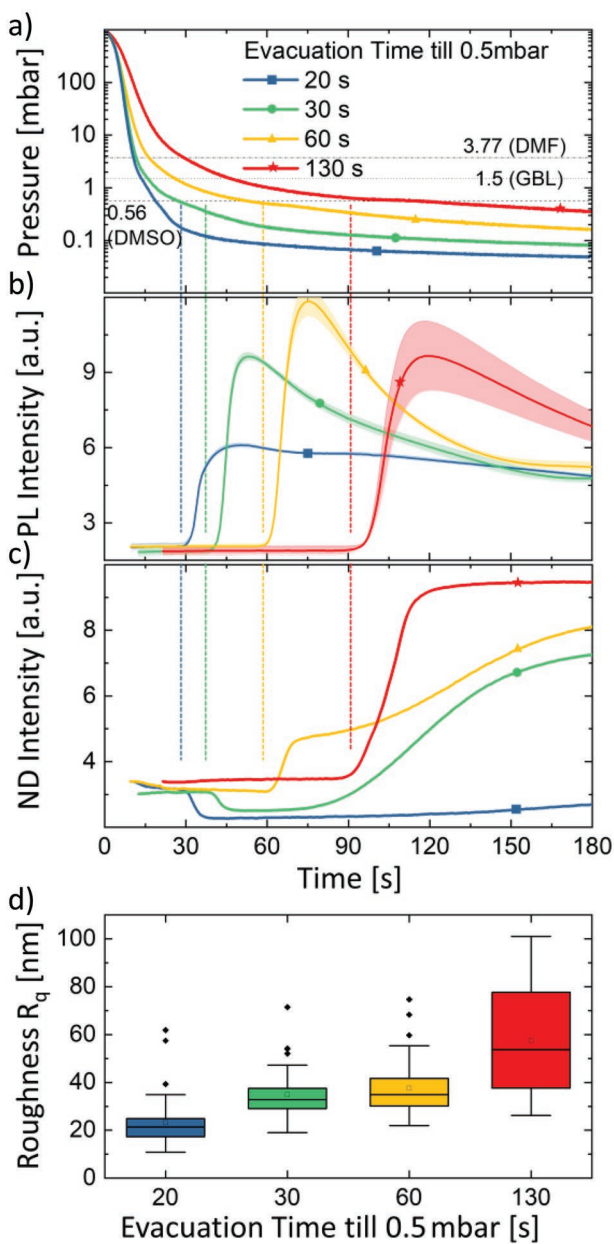


Figure 3. a) Process pressures of a vacuum chamber loaded with a blade-coated substrate ($32 \times 64 \text{ mm}^2$, $\approx 25 \mu\text{L}$) at different evacuation rates (time till 0.5 mbar is reached). Indicated are the vapor pressures at 20°C of the three apparent solvents DMF, DMSO and GBL; b) LP725-channel and c) ND-channel transients of the inner active areas; d) RMS roughness R_q of the inner areas of these substrates after annealing extracted from profilometry.

(Figure 3b). The slower drying affects the crystallization itself, changing the morphology of the perovskite thin-film. This leads to a gradual change in the reflection signal (Figure 3c). The standard deviation is shown in Figure S13, Supporting Information. The increase in reflection correlates with the increasing film roughness for slower drying films (see macroscopic roughness in Figure 3d) and the different surface formation (see AFM surfaces and microscopic roughness in Figure S14, Supporting Information, which might have an effect

on the absorption coefficients). With increasing roughness of the surfaces at slower evacuation rates, pinholes as well as needle-like crystallites (which could be PbX_2) appear. Additionally, buried voids could appear at the bottom of the thin-film as result of slow DMSO evaporation changing the reflection signal gradually.^[67] These affect the device performance, lowering the PCE from >14% for fast evacuation to <7% for slow one (see Figure S15, Supporting Information). The trend is in good agreement with the findings in ref. [50], where IJP C_5 -TCP wet-films of similar thickness ($\approx 11.2 \mu\text{m}$ vs $\approx 12.2 \mu\text{m}$)¹ calculated from 300 dpi, 80 pL, $25 \times 25 \text{ mm}^2$ and $32 \times 64 \text{ mm}^2$, 25 μL crystallize after around 200 s (final pressure $\geq \approx 0.5$ mbar), demonstrating high pinhole density, incomplete film formation, and low device performance. These results indicate that similar to gas flow quenching,^[48,68] the key to control the formation of high quality perovskite thin-films with VAG is a fast drying rate, which can be achieved by fast evacuation below the vapor pressures of the ink's solvents or by an additional gas flow inside the chamber to enhance the drying rate.^[50] The formation of slowly dried and therefore rough DCP thin-films and fast crystallized smooth DCP surfaces can be distinguished by observing the reflection channel and process pressure.

3.2.2. Nucleation On-Set: Wet-Film Thickness

For a given ink system and vacuum chamber, the wet-film thickness should influence the nucleation on-set and is therefore investigated. We use inkjet printing to maintain precise control over the deposited volume and area. While monitoring the drying of six IJP squares of different resolution and thereby of wet-film thickness (see Table S2, Supporting Information), a prominent shift in PL on-set time is apparent (see Figure 4a for image data and Figure 4b for transients of the mean central area of the SP775 channel). The thicker the wet-film thickness, the longer is the evaporation process and the nucleation and PL on-set is delayed. To account for the drying induced ink movements, for example, to create coffee rings at the edge of the square, the PL on-set time is shown depending on the dry-film thickness after VAG and thermal annealing (see Figure 4c). The linear fit highlights the correlation between the on-set time and the final thickness. It should be noted that the dependence of the printing resolution in dpi and the calculated wet-film thickness is quadratic and not linear. Shortly after the PL on-set, the PL intensity reaches a maximum peak and the height of the maximum decreases with the initial wet-film thickness, as it is shown in Figure 4d spatially on images and Figure 4e as transients. At the time of the PL peak, the concentration of crystallites might reach a maximum while the thin-film still contains solvent residuals, hindering the excited charge carriers to be extracted. With progressing evacuation time, the crystallites grow and coalesce, facilitating charge carrier extraction and decreasing radiative recombination. With thicker wet-film thickness, the relative penetration depth of the excitation light compared to the absolute thickness is reduced and the self-absorption of the emitted PL is increased, lowering the PL intensity. Independent of the exact mechanism, the PL intensity correlates negatively to the dry-film thickness for the investigated thickness range, measured after VAG and

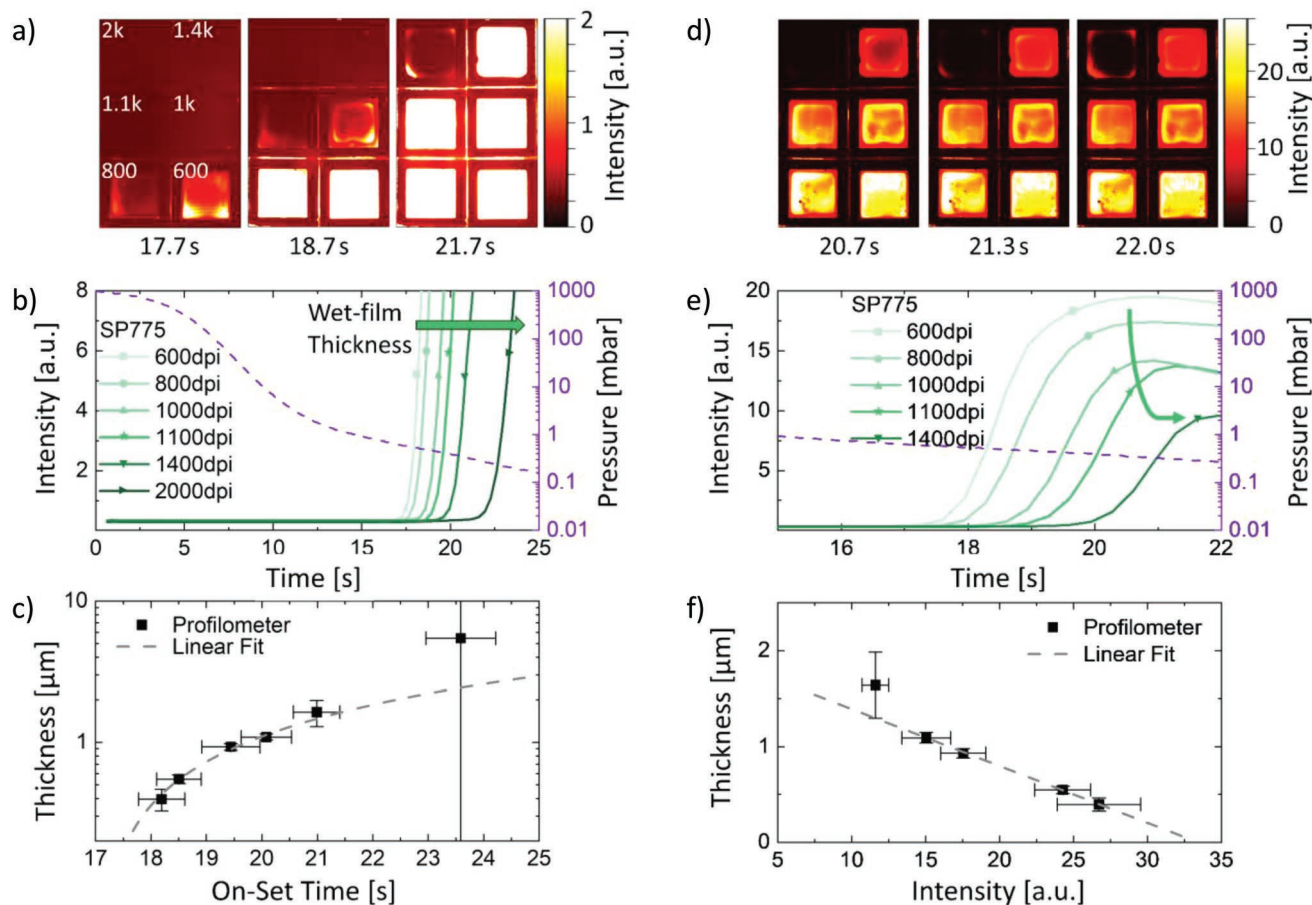


Figure 4. a) SP775-channel images of inkjet-printed squares of different resolution in dpi at different times showing their PL on-set; b) Transient mean intensity of the inner area of these squares while initial chamber evacuation till their PL on-set; c) Layer thickness of fully annealed samples in comparison to their PL on-set time. d) Same squares as in (a) at the period of their intensity peak after the PL start; e) Transients of (d) till the initial PL maximum is reached; f) Layer thickness of fully annealed samples in comparison to their maximum intensity after their PL start.

thermal annealing and can be used to predict the thin-film in situ (Figure 4f).

The remaining PL channels exhibit similar trends (see Figure S16, Supporting Information). The SP775 channel in Figure 3 is chosen, since the signal includes the earliest PL on-set due to the highest transmission in the initial PLs spectral range. In contrast, the LP725 channel shifts in time due to the low transmission in the below 725 nm WL range and consequently lower signal to noise ratio. The LP780 signal on-set depends on the red-shift during the crystallization and is therefore not suitable for identification of the thickness. The ND channel signal drops once the perovskite formation starts due to the absorption increase which is visible by eye. The reflection drop on-set is shifted similar to the PL on-set depending on the wet-film thickness.

Although the PL on-set is a good measure for the film thickness, the substrate and layer stack below the wet-film simultaneously influence the PL on-set. For glass/ITO/NiO_x substrates with and without an additional 2PACz layer, the on-set is shifted and the maximum PL peak intensity is lower, but the overall wet-film thickness trend persists although different wetting on both surfaces slightly influences the final layer thickness (see Figure S17a,b, Supporting Information).

A reason for this could be different charge carrier extraction within the crystallites in the wet-film or different nonradiative interface recombination that quenches the PL signal below the detection limit and delaying the PL on-set.

In summary, assuming a constant ink system and VAG process, the thin-film thickness can be estimated when using consistent substrate material or the relative charge carrier extraction by employing the same perovskite thickness and changing the substrate material.

3.3. Phase II: Nucleation and Crystal Growth

3.3.1. Wet-Film Thickness Dependent Crystallization

Besides the PL intensity and on-set, spectral information is required to monitor the crystallization. As shown for IJP C₁₀-TCP,^[23] varying wet-film thicknesses lead to a differently crystallized thin-film (less conversion for thinner films) and different stoichiometric compositions on the perovskites surface annealed by VAG. Consequently, monitoring VAG reveals changes in the thin-film formation. Extracting the PL peak WL for IJP DCP thin-films of different resolutions shows indeed

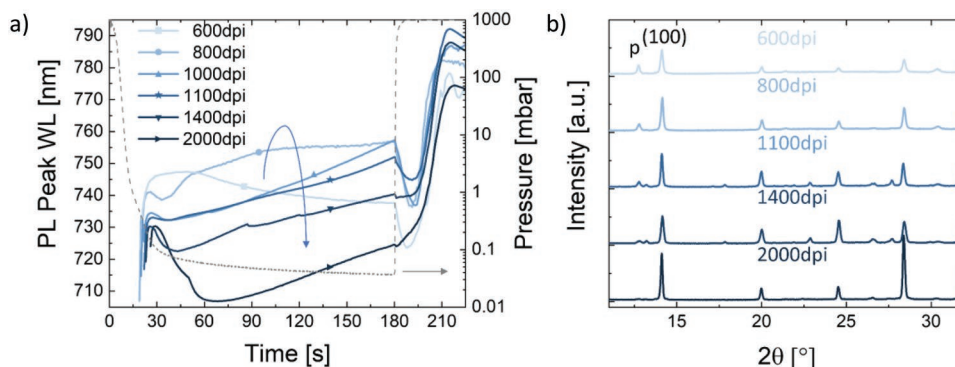


Figure 5. a) PL peak wavelength (WL) development over time of inkjet-printed DCP thin-films with different printing resolution in dpi and b) corresponding XRD patterns. p indicates the (100) PbX_2 peak and (100) the CFP (100) peak.

a different behavior depending on the wet-films thickness (see Figure 5a). After a fast red-shift, assumedly due to the growth of the nuclei for all resolutions, the shape of the PL peak WL transients changes. The PL peak WL shifts toward higher WL after an initial blue-shift until the thin-film is dry, as it is the case for the 600 dpi and 800 dpi films (shown below).

The shift is attributed to slow incorporation of ions (e.g., Γ^- or FA^+) as long as there are solvent residuals inside. X-ray diffraction (XRD) patterns show similar PbX_2 to (100) DCP peak ratio trends as C_{10} -TCP for different wet-film thicknesses,^[23] indicating that higher solvent residuals lead to a more complete formation (see Figure 5b for XRD patterns and Figure S23, Supporting Information, for the peak ratios).

3.3.2. Evacuation Time and Venting

The VAG time^[69] and the venting itself^[50] are known to impact the VAG-induced crystallization and morphology of perovskite thin-films. Therefore, it is important to know and to control the dry-state of the perovskite films, that is, the solvent residuals in the perovskite films. The extraction of the solvent residuals in the perovskite film during VAG is enhanced either by applying vacuum for a longer period or inducing a gas flow while venting. To investigate the influence of the solvent extraction time, the VAG process is stopped after 1 min, 3 min, and 10 min while monitoring the thin-films with the imaging setup. Figure 6 a,b shows the PL intensity and reflection transients, normalized to the intensity at the time of venting. Corresponding images at the time of venting and 60 s after of IJP DCP squares aligned at the point in time when the venting is initiated are shown in Figures 6c and 6d, respectively. While the PL intensity and reflection both show an oscillation for the short VAG times and increases after, it flattens respectively and stays constant for longer evacuation times. With the solvents removed, the film is dry and rigid, while the short annealing time still leaves residuals and the surface changes upon venting. This is shown for wet-films of different resolutions for the three evacuation times in Figure S18, Supporting Information, together with the corresponding PL peak WL transients in Figure S19, Supporting Information and for the case venting before nucleation has started in Figure S20, Supporting Information. While after 1 min VAG only the 600 dpi squares PL

(ND) signal remains low (at a similar intensity level), the signals decrease stepwise for all but 1400 dpi and 2000 dpi after 10 min evacuating. Depending on evacuation time and wet-film thickness, a dry-state of the perovskite film after VAG is reached when the reflection signal remains low, meaning the surface morphology does not change upon venting. The PL intensity increases only for incompletely dried films, presumably because of the increase in surface roughness occurring at the time of the oscillation which will influence the final surface roughness (see Figure 6e). This is attributed to a change in SFT of the solvent residuals in the thin-film with increasing pressure. The change in surface roughness while venting is depicted in Figure S21, Supporting Information, in particular for the 2000 dpi case with the highest initial wet-film volume. While the SFT is known to be dependent on (over-)pressure and surrounding gas,^[70–72] it is difficult to measure the SFT change in the wet-film inside the vacuum chamber. In contrast when venting with an additional nitrogen flow, the PL intensity and the reflection and therefore surface roughness remain constant for all wet-film thicknesses (see Figure S22, Supporting Information). The surface roughness even for the thickest 2000 dpi wet-film is smooth (see Figure S23, Supporting Information), indicating that the constant nitrogen flow increases the drying rate and that the PL intensity increase originates from the surface morphology change.

The influence of the drying time is also apparent in X-ray diffraction patterns (see Figure 6f). Thin-films annealed for shorter evacuation time exhibit an additional peak at a diffraction angle of $2\theta \approx 9.9^\circ$ and $2\theta \approx 13.2^\circ$ (and some at higher angles, shown in patterns of wider diffraction angle range for different printing resolutions and the three evacuation times in Figure S24, Supporting Information). The peak at $\approx 9.9^\circ$ is attributed to $\text{PbX}_2(\text{DMSO})$ or $\text{PbX}_2(\text{DMSO})_2$ complexes,^[65,73,74] but also (δ) - CsPbI_3 phases occurring in $\text{Cs}_y\text{FA}_{1-y}\text{PbI}_3$ films for higher y ^[75,76] could be possible. The peak at $\approx 13.2^\circ$ and peaks at larger angles agree with those reported for CsPbI_3 phases. Independent of the origin, the peaks seem to correlate with the dry-state of the film as depicted in Figure S25a,b, Supporting Information, for the intensity of the 9.9° and 13.2° peak. For very thick thin-films as in the 2000 dpi case, we assume the peak height to be less than the detection minimum. It should be noted, that as shown for C_{10} -TCP,^[23] the crystallization and more specific the PbX_2 residuals in the thin-film depend on

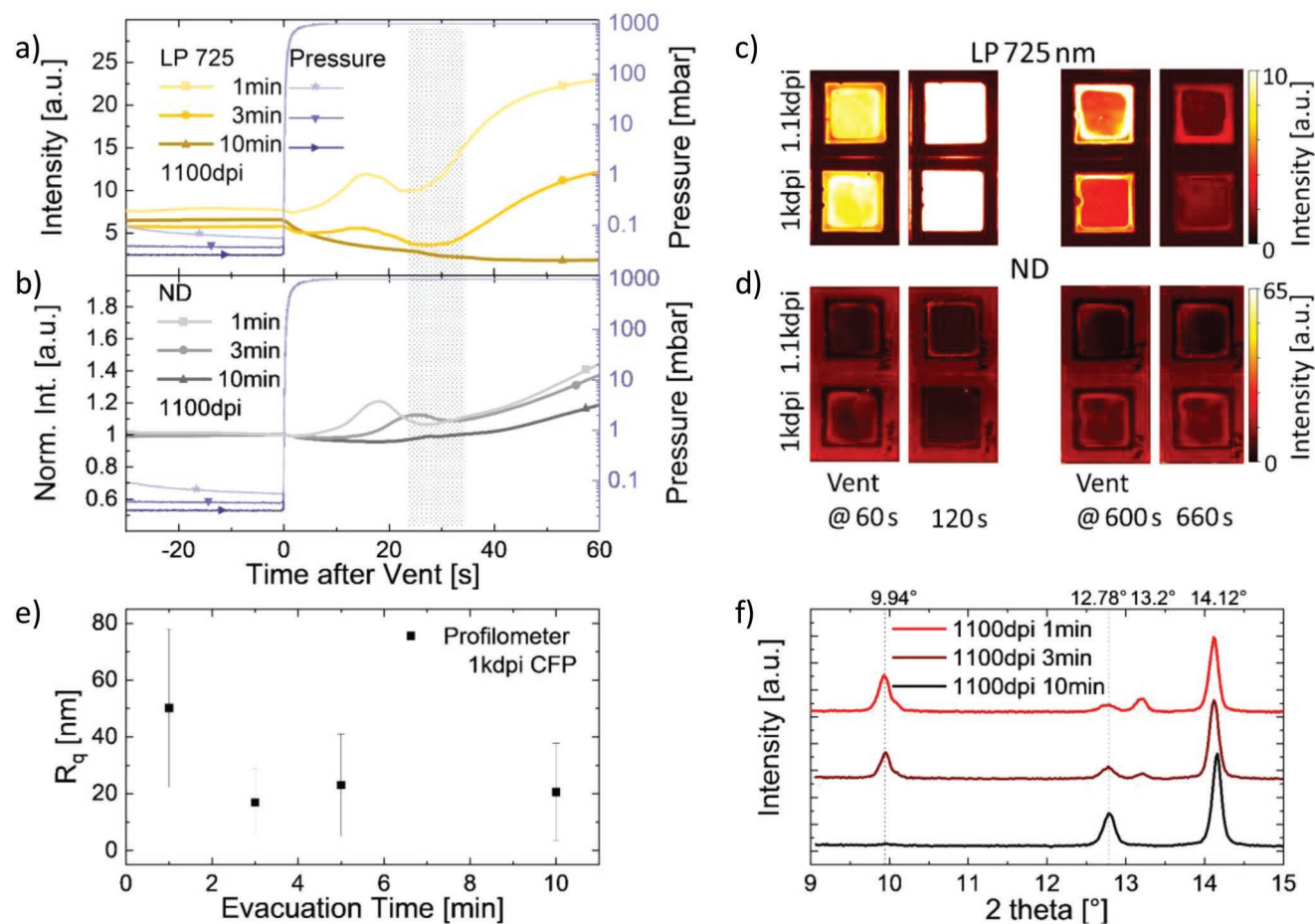


Figure 6. Transient intensity of the a) LP725- and b) the ND-channel around the time of venting for inkjet-printed 1100 dpi squares evacuated for 1, 3, and 10 min and corresponding process pressures. The shaded area indicates the time when the chamber pressure is at ambient atmosphere again. Images of an inkjet-printed 1000 dpi and 1100 dpi square at the time of venting and 60 s later for short (1 min) and long (10 min) evacuation time of the c) LP725-channel and d) the ND-channel; e) RMS roughness the active areas of 1000 dpi squares depending on the evacuating time; f) X-ray diffractograms of the three substrates shown in (a) with indicated peak positions.

the initial wet-film thickness (see Figure S25c,d, Supporting Information). In summary, the initial wet-film thickness and the dry-state of the thin-film influence the crystallization and morphology, and can be monitored by means of spatial PL and reflection. In agreement with ref. [50], the venting plays a vital role in the final film morphology and has an effect on the crystallization.

3.3.3. Thermal Annealing

The final stage of VAG is thermal annealing which ends phase II, nucleation and crystal growth. We only monitor the first minutes of thermal annealing since DCP forms already during VAG and within this period the PL is nearly completely quenched (see above and compare ref. [49]). The PL intensity shape after quenching appears comparable, but depends on the thin-film thickness, presumably more precise on the amount of solvent residuals. The PL intensity transients' decay of IJP DCP squares of different resolution (see Figure S26a, Supporting Information) starts at similar times, but the period till the minimum is reached is longer and the signal intensity remains

high. Moreover, films of the same resolution that are in vacuum for evacuation times between 1 min and 10 min or that are annealed at annealing temperatures between 100 and 150 °C, reveal the same trend (see Figure S26b,c, Supporting Information): the duration between contact with the hotplate and the point in time at which the PL intensity reaches the minimum is longer for films with shorter vacuum times, that is, higher solvent residuals, and at lower temperature, where the solvent evaporation rate is slower. The suspected higher amount of solvent residuals in the film or slower removal rate is presumed to delay the final formation and hinder a fast charge carrier transport into HTL and ITO causing the delayed minimum.

3.4. Correlation of In Situ Data and Solar Cell Properties

Finally, we employ the demonstrated correlations and insights to highlight potential applications: the PL on-set time is correlated to the wet-film and dry-film thickness and thus the performance of solar cells is affected. Blade-coated (bc) DCP ink on glass/ITO/ NiO_x /bc-2PACz substrates are therefore monitored during VAG and the PL on-set time of each mean SP775

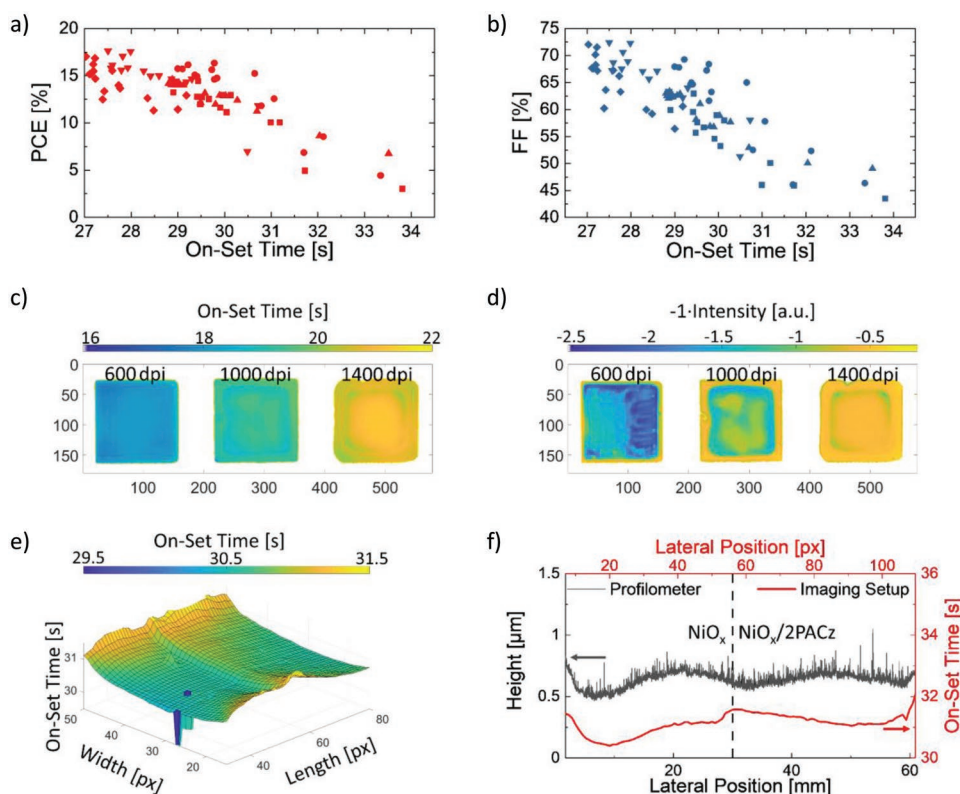


Figure 7. a) Power conversion efficiency (PCE) and b) fill factor (FF) sorted according to their PL on-set time of the SP775-channel of four blade-coated DCP substrates with 16 active areas each; c) PL on-set time and d) inverse maximum intensity after PL on-set surface map of inkjet-printed squares of different resolution extracted from the LP725-channel; e) PL on-set time 3D surface map of blade-coated DCP on ITO/NiO_x (left front side, till length ≈ pixel 58) and ITO/NiO_x/bc-2PACz (right back side, from length pixel ≈ 58 on) and f) comparison of the profiles along this substrates central y-coordinate between a profilometer and the PL on-set time data. Indicated is the approximate position where the 2PACz is blade-coated (center to right), the DCP ink is blade-coated from right to left. In (c) and (d), the outcoupled PL at the substrate edges is cut out.

intensity transient of the active areas is extracted. The PCE and fill factor sorted according to their PL on-set time is shown in **Figure 7a,b**. To minimize the influence of manufacturing steps after the monitored VAG process, we finalized the solar cell architecture with a thermally evaporated C₆₀-fullerene/bathocuproine (BCP)/Ag sequence. As the film thickness increases, the PL on-set time increases and the FF decreases along with the PCE (short-circuit current density J_{sc} and open-circuit voltage V_{oc} over PL on-set time are shown in Figure S27, Supporting Information). Although the device performance and mean value of the PL on-set time correlate, the statistical deviation is quite high. We are confident that the correlation can be increased by including more parameters than the mean value of the active area of the PL on-set of one filter channel (e.g., median to mean ratio or standard deviation for homogeneity of the active area, combining points of interest of above discussed findings, combining ND and PL channels).

Instead of mean values of areas, the transients of each individual pixel on the image can be analyzed to obtain characteristic values of interest. Figure 7c shows the LP725 on-set times of each pixel of six with different resolution IJP squares and Figure 7d the maximum intensity (before venting) of the same squares. As both values of interest exhibit a wet-film thickness correlation, a 3D shape of the films during VAG is created (3D map shown in Figure S28, Supporting Information). Both maps

differ, as the thickness is not the only influencing parameter and can be used as homogeneity indicator. The edge areas of each square emit PL in non-normal direction and should be excluded.

Moreover, HTL differences can be detected with the same approach. A PL on-set time map of a bc DCP film on top of a glass/ITO/NiO_x/substrate halfway coated with a 2-PACz layer is shown in Figure 7e. The clearly visible step is depicted as cross-sectional comparison between profilometer and PL on-set time map in Figure 7f. While in the profile no hint of two different HTLs is detected, the PL on-set cross section shows it clearly.

In summary, the PL and reflection imaging system is suitable for monitoring VAG processes and collecting spatial information of the drying and crystallization process. The data is used for an estimation of the film thickness and morphology and combined with the ability to detect holes by the imaging setup as it is shown in ref. [51] and as in Figure 7e, an in situ tool for quality control for the performance of printed and coated perovskite solar cells is presented.

4. Conclusion

In this work, we demonstrate a facile multichannel photoluminescence and reflection imaging system for in situ monitoring

of film formation and crystallization of lead halide perovskite thin-films during vacuum-assisted growth control (VAG) and subsequent thermal annealing. We discuss the requirements of standard perovskite compositions (minimum Cs-content or applied heat is needed) for photo-active film formation during VAG. On the basis of the exemplary state-of-the art $\text{Cs}_{0.17}\text{FA}_{0.83}\text{Pb}(\text{I}_{0.91}\text{Br}_{0.09})_3$ (DCP) composition, we discuss in detail key parameters of the VAG process for inkjet-printed and blade-coated DCP thin-films using our spatial imaging analysis. We highlight insights into the perovskite formation process depending on the evacuation rate, which is found to be essential if no additional gas flow is applied. Furthermore, we identify PL and reflection channel features and points of interest, correlating with surface roughness, film thickness, and dry state of the thin-films. Altogether, the detectability of these features for DCP allow in situ process control and can be used in the future for automated production line integration.

5. Experimental Section

Ink Fabrication: The inks for blade coating, inkjet printing, and drop casting were prepared as follows: For the DCP perovskite ink, PbI_2 (0.875 M, TCI Chemicals), and PbBr_2 (0.125 M, TCI Chemicals) were dissolved in a mixture of DMF (anhydrous, Sigma-Aldrich), DMSO (anhydrous, Sigma-Aldrich) in a ratio 4:1 (volume percentage). The PbX_2 solution was then added to $\text{CH}(\text{NH}_2)_2\text{I}$ (FAI, 0.825 M, GreatCell Solar) and CsI (0.175 M, abcr) and diluted 2:1 vol:vol with GBL (Sigma-Aldrich). MAPbI was prepared by dissolving PbI_2 (1 M) and then $\text{CH}_3\text{NH}_2\text{I}$ (MAI, GreatCell Solar) with the PbI_2 solution and diluting the same way. $\text{Cs}_{0.17}\text{FA}_{0.83}\text{Pb}(\text{I}_{0.91}\text{Br}_{0.09})_3$ ink was mixed from an $\text{FAPbI}_{2.73}\text{Br}_{0.27}$ and a DCP ink in the stated volume ratio. $\text{CsCl}_{0.17}\text{FA}_{0.83}\text{PbI}_3$ was prepared according to ref. [77] and diluted 2:1 vol:vol with GBL. Triple cation perovskite ink was prepared as described in refs. [16,23]. For all inks, 2.4 vol% L- α -phosphatidylcholine (Sigma-Aldrich) solution (0.5 mg mL⁻¹ in DMSO) was added before use.

Sample Fabrication: Pre-patterned ITO on glass substrates for devices, non-patterned ITO for characterization samples (Luminescence Technology), and textured Si substrates (Singulus Technologies; anisotropically etched n-type, monocrystalline <100> silicon wafers) were cleaned consecutively in acetone and isopropanol (IPA) in an ultrasonic bath for 10 min each, followed by an oxygen plasma cleaning step for 3 min. Another cleaning step in acetone and IPA was needed for appropriate wetting behavior in case the perovskite was IJP on pure glass/ITO.

The textured Si samples were insulated with a 50 nm thick Al_2O_3 film deposited by atomic layer deposition (Picosun R200, 750 cycles at 80 °C with trimethylaluminum and water as precursor materials and Argon as carrier gas) and then a 135 nm thick ITO thin-film was sputtered at 250 W from an ITO target (Kurt J. Lesker Company, 99.99% purity) through a shadow mask using a Pro Line PVD-75 thin-film deposition system (Kurt J. Lesker Company) as described in detail in ref. [78]. As process gas, 96.5% Ar with 3.5% O₂ at a pressure of 0.8 mTorr was used.

NiO_x HTL layers with 10 nm (15 nm for Si substrates) layer thickness were sputtered at 1 mTorr process pressure with Ar as process gas at 100 W under rf-conditions from a NiO_x target (Kurt J. Lesker Company, 99.995% metallic purity) as in ref. [3].

After a short low power oxygen plasma treatment, a 2PACz solution (>98%, TCI Chemicals), 0.375 mg mL⁻¹ (for spin coating) and 1.5 mg mL⁻¹ (for blade coating) in ethanol (99.8%, VWR) was coated on top. For substrates intended for an IJP perovskite layer, 2PACz was spin-coated in a nitrogen-filled glovebox (3000 rpm, 1000 rpm s⁻¹, 30 s) as described in ref. [79] and annealed for 10 min at 100 °C. Blade coating was done with a Zehntner ZAA 2300.H automatic film applicator and a ZUA 2000 universal applicator. The blading gap was set to 100 μm

and after pipetting 16 μL ink into the gap, the substrate was coated at a blade speed of 16 mm s⁻¹ two times in forward direction and annealed for 10 min at 100 °C. All inkjet printing, blade coating, and successive annealing steps were performed in ambient conditions (≈21 °C, 45% relative humidity).

A Meyer Burger/Süss MicroTec PiXDRO LP50 with a print head module for 10 pl Fujifilm cartridges (Dimatix DMC-16610) was used for inkjet printing. The perovskite absorber layers were deposited similarly as described in refs. [23,52] at 2–5 kHz jetting frequency independent of the resolution. Typically, the printed area was 11 × 11 mm² per 16 × 16 mm² sample and the four active areas would be within the inner 8.5 × 8.5 mm² square.

The blade coating parameters for the perovskite absorber layers were set to 100 μm blading gap, 25 μL ink volume, and 25 mm s⁻¹ blading speed. The sample size was typically 32 × 64 mm² and the substrate backside was marked with the later substrate size of 16 × 16 mm² prior cleaning.

The as-coated samples were transferred within 90 s after the deposition process to a self-build vacuum chamber (specifics below) which was then evacuated. After the chamber was vented, the samples were put on a hotplate at 150 °C for annealing.

The completed blade-coated samples were cut into 16 × 16 mm² samples.

Finally, a 25 nm C₆₀ fullerene (Sigma-Aldrich, 98%) ETL, a 5 nm BCP (Luminescence Technology) interfacial layer, and 100 nm silver back-contact defined by a shadow mask were thermally evaporated. This defined the active area to 10.5 mm² per solar cell with 4 cells.

Vacuum Chamber and Tracking: The cuboidal vacuum chamber was made of stainless steel with an empty capacity of ≈3.34 dm³, one evacuating valve (≈25 mm diameter), and venting inlet (≈5 mm diameter) on the opposing side. A Pirani-type pressure sensor (Leybold Heraeus) was mounted between valve and chamber. The sensor's analog voltage output (Thermovac TM 210S) was read-out time sensitive by a micro controller and translated to a corresponding pressure. The starting point t_{p0} for each experiment was set to the first detected change in voltage. The lid of the chamber was made from Plexiglas, where the PL imaging setup was placed upon. The chamber had a modular layout wherefore a feedthrough for optical fibers for a spectrometer or one for an electrical sensor and power cables for temperature measurements (Pt100 sensors) and a microcontroller-operated Peltier element could be applied. The evacuation rate was controlled with an additional throttle which decreased the tube diameter directly after the valve. The chamber was vented with surrounding air unless noted otherwise. The substrates were placed far away from gas inlet of the vacuum chamber to reduce the impact of inhomogeneities in the gas flow during pump down and venting. The chamber geometry and volume were expected to impact the optimum pump down times, etc., however using two very different chambers, similar performance and thin film quality were obtained after optimization.

Photoluminescence Imaging Setup: The setup was based on and partly identical to the one described in detail in ref. [51]. A monochrome sCMOS camera (CS2100M-USB Quantalux, Thorlabs) with mounted lens (MVL25M23, focal length 25 mm, field of view 24.3°, or MVL12M23, focal length 12 mm, field of view 46.8°, both Thorlabs) was capturing 2.1-megapixel (1920 × 1080 pixels, resulting in ≈0.08 mm/px and ≈0.06 mm/px resolution, respectively, for the given work distance and mounted lens) images triggered by a microcontroller. The trigger was synchronized with a black filter wheel rotating at a speed of 180 rpm, resulting in a framerate of 3 fps per channel and in an ≈0.08 s (for the two neighboring filters) to 0.17 s (for the opposite filter) delay between frames of two channels (delay time depends on the filter position in the wheel). The exposure time was 10 ms. The filter wheel was loaded with two longpass filters (at 725 nm (Edmund Optics, stacked below a RG620 filter to cut low wavelength transmission) and at 780 nm (RG780, Thorlabs, stacked on top of a RG715 filter to cut low wavelength transmission)), a bandpass filter realized with a stacked short- and longpass (between 665 nm (RG665, Thorlabs) and 775 nm (Edmund Optics)) and an ND filter (two stacked linear polarizers LPVISE200-A,

Thorlabs) with adjustable transmittance. The filter set (their transmittance is shown in Figure S1c,d, Supporting Information) was chosen for a Gaussian-like PL emission profile with a central wavelength $\lambda_{\text{center}} = 780$ nm and to cut the excitation light. Two LDL2 (146 × 30BL2-WD) blue LED bars (CCS Inc., $\lambda_{\text{center}} = 467$ nm, FWHM ≈ 28 nm, mounted in parallel, facing each other and tilted in an $\approx 45^\circ$ angle toward the substrate surface to avoid reflections from the LEDs themselves) were used for excitation with an irradiance around 0.08 suns. This led to a slight temperature increase in the vacuum chamber of 0.3 °C, but no detrimental change was observed in device performance (see Figure S29, Supporting Information). The ND images pictured the intensity of the reflected excitation light, the LP725 measured the PL intensity, and the PL peak WL was extracted via a model introduced by ref. [56]. The ratios of the background-corrected LP725, LP780, and SP775 images were taken and compared to a look-up table created with Gaussians representing PL emission profiles while considering the optical transmittance data of filters, lenses, and camera. Images and pressure profile were aligned at the start of the vacuum chamber evacuation t_{p0} . The PL on-set time was extracted at an arbitrary chosen threshold intensity above the noise level for each channel. For the 2D and 3D surface maps the transients of each pixel were used for the calculation, for device performance and topography comparisons the mean value of the active area(s) was used.

In Situ Photoluminescence Spectrometry: A wavelength- and intensity-calibrated HDX-XR spectrometer (Ocean Optics) was connected via an optical fiber feedthrough to a mount 45° -tilted toward the substrate surface inside the vacuum chamber. A RG600 filter in front of a collecting lens was used to cut the excitation light. The integration time was set to 3 s, the acquired spectra were background-corrected. The PL peak wavelength was extracted from a Gaussian fit through each spectrum.

Atomic Force Microscopy: The surface profiles were measured using a NanoWizard II (JPK Instruments) and the data was background-corrected with a second-degree polynomial fit function.

X-Ray Diffractometry: The XRD patterns were measured using a Bruker D2 PHASER (Cu K- α radiation) and aligned at the ITO (222) peak ($2\theta = 30.5^\circ$) to correct for small drifts.

Profilometry: A Dektak XT stylus profilometer (Bruker) was used for lateral profiles and the acquired data was corrected with a second-degree polynomial fit function, before extracting thickness and roughness information from the active area region.

UV-Vis-NIR Spectrophotometry: Total transmittance and reflectance were measured with a Lambda 1050 spectrophotometer (PerkinElmer) with an integrating sphere. Diffuse reflectance was measured with an open integrating sphere at the angle of direct reflection. The specular reflectance was calculated according to $R_{\text{specular}} = R_{\text{total}} - R_{\text{diffuse}}$.

Solar Cell Characteristics: A class AAA 21-channel LED solar simulator (Wavelabs Solar Metrology Systems Sinus-70) with an AM1.5G spectrum (100 mW cm^{-2}) inside a nitrogen-filled glovebox was used for measuring the solar cell characteristics. The intensity was calibrated with a KG5 bandpass-filtered silicon reference solar cell (Newport). JV-scans of the cells were measured in both backward and forward direction (constant scan rate of $\approx 0.6 \text{ V s}^{-1}$, Keithley 2400 source measurement unit). The temperature of the solar cell was controlled at 25 °C using a microcontroller-supervised Peltier-element for both JV-scans and MPP measurements.

Supporting Information

Supporting Information is available from the Wiley Online Library or from the author.

Acknowledgements

The financial support by the Federal Ministry for Research and Education (BMBF) through the project PRINTPERO (03SF0557A); the Federal Ministry of Economics and Technology (BMWK) through the project

CAPITANO (03EE1038B); the European Union's Horizon 2020 research and innovation program through the project PERCISTAND (850937); the Initiating and Networking Funding of the Helmholtz Association (HYIG of U.W.P. (VH-NG-1148)) and Helmholtz Association program: Program oriented funding IV, Materials and Technologies for the Energy Transition, Topic 1: Photovoltaics and Wind Energy (38.01.03); the Deutsche Forschungsgemeinschaft (DFG, German Research Foundation) under Germany's Excellence Strategy via the Excellence Cluster 3D Matter Made to Order (EXC-2082/1-390761711); and the Karlsruhe School of Optics & Photonics (KSOP) is gratefully acknowledged. The authors would like to thank the members of the Perovskite Taskforce at LTI and the Printed Electronics research group at InnovationLab for fruitful discussions and support in the authors' scientific work, Simon Ternes for helpful discussions, Hang Hu and Thomas Feeney for developing and performing the ALD deposition, and Tobias Abzieher for developing the NiO_x sputtering process.

Open access funding enabled and organized by Projekt DEAL.

Conflict of Interest

The authors declare no conflict of interest.

Author Contributions

The manuscript was written through contributions of all authors.

Data Availability Statement

The data that support the findings of this study are available from the corresponding author upon reasonable request.

Keywords

blade coating, inkjet printing, in situ optical monitoring, perovskite solar cells, photoluminescence, vacuum quenching

Received: August 12, 2022

Revised: September 27, 2022

Published online:

- [1] C. Li, Y. Ma, Y. Xiao, L. Shen, L. Ding, *InfoMat* **2020**, 2, 1247.
- [2] Y. C. Kim, K. H. Kim, D.-Y. Son, D.-N. Jeong, J.-Y. Seo, Y. S. Choi, I. T. Han, S. Y. Lee, N.-G. Park, *Nature* **2017**, 550, 87.
- [3] H. Mescher, F. Schackmar, H. Eggers, T. Abzieher, M. Zuber, E. Hamann, T. Baumbach, B. S. Richards, G. Hernandez-Sosa, U. W. Paetzold, U. Lemmer, *ACS Appl. Mater. Interfaces* **2020**, 12, 15774.
- [4] G. Pacchioni, *Nat. Rev. Mater.* **2021**, 6, 108.
- [5] W. S. Yang, B.-W. Park, E. H. Jung, N. J. Jeon, Y. C. Kim, D. U. Lee, S. S. Shin, J. Seo, E. K. Kim, J. H. Noh, S. I. I. Seok, *Science* **2017**, 356, 1376.
- [6] National Renewable Energy Laboratory (NREL). Best Research-Cell Efficiency Chart.
- [7] T. Abzieher, T. Feeney, F. Schackmar, Y. J. Donie, I. M. Hossain, J. A. Schwenzer, T. Hellmann, T. Mayer, M. Powalla, U. W. Paetzold, *Adv. Funct. Mater.* **2021**, 31, 2104482.
- [8] C. Bi, Q. Wang, Y. Shao, Y. Yuan, Z. Xiao, J. Huang, *Nat. Commun.* **2015**, 6, 7747.

- [9] N. J. Jeon, J. H. Noh, Y. C. Kim, W. S. Yang, S. Ryu, S. I. I. Seok, *Nat. Mater.* **2014**, *13*, 897.
- [10] G. Jang, H. Kwon, S. Ma, S. Yun, H. Yang, J. Moon, *Adv. Energy Mater.* **2019**, *9*, 1901719.
- [11] S. Sanchez, N. Christoph, B. Grobety, N. Phung, U. Steiner, M. Saliba, A. Abate, *Adv. Energy Mater.* **2018**, *8*, 1802060.
- [12] K. Bruening, B. Dou, J. Simonaitis, Y.-Y. Lin, M. F. A. M. van Hest, C. J. Tassone, *Joule* **2018**, *2*, 2464.
- [13] S. Ternes, T. Börnhorst, J. A. Schwenzer, I. M. Hossain, T. Abzieher, W. Mehlmann, U. Lemmer, P. Scharfer, W. Schabel, B. S. Richards, U. W. Paetzold, *Adv. Energy Mater.* **2019**, *9*, 1901581.
- [14] Y. Yu, F. Zhang, T. Hou, X. Sun, H. Yu, M. Zhang, *Sol. RRL* **2021**, *5*, 2100386.
- [15] L. Gu, F. Fei, Y. Xu, S. Wang, N. Yuan, J. Ding, *ACS Appl. Mater. Interfaces* **2022**, *14*, 2949.
- [16] F. Mathies, H. Eggers, B. S. Richards, G. Hernandez-Sosa, U. Lemmer, U. W. Paetzold, *ACS Appl. Energy Mater.* **2018**, *1*, 1834.
- [17] B. Abdollahi Nejand, I. M. Hossain, M. Jakoby, S. Moghadamzadeh, T. Abzieher, S. Gharibzadeh, J. A. Schwenzer, P. Nazari, F. Schackmar, D. Hauschild, L. Weinhardt, U. Lemmer, B. S. Richards, I. A. Howard, U. W. Paetzold, *Adv. Energy Mater.* **2020**, *10*, 1902583.
- [18] J. Kim, J. S. Yun, Y. Cho, D. S. Lee, B. Wilkinson, A. M. Soufiani, X. Deng, J. Zheng, A. Shi, S. Lim, S. Chen, Z. Hameiri, M. Zhang, C. F. J. Lau, S. Huang, M. A. Green, A. W. Y. Ho-Baillie, *ACS Energy Lett.* **2017**, *2*, 1978.
- [19] J. A. Schwenzer, T. Hellmann, B. A. Nejand, H. Hu, T. Abzieher, F. Schackmar, I. M. Hossain, P. Fassel, T. Mayer, W. Jaegermann, U. Lemmer, U. W. Paetzold, *ACS Appl. Mater. Interfaces* **2021**, *13*, 15292.
- [20] C. C. Boyd, R. Checharoen, T. Leijtens, M. D. McGehee, *Chem. Rev.* **2019**, *119*, 3418.
- [21] I. A. Howard, T. Abzieher, I. M. Hossain, H. Eggers, F. Schackmar, S. Ternes, B. S. Richards, U. Lemmer, U. W. Paetzold, *Adv. Mater.* **2019**, *31*, 1806702.
- [22] F. Mathies, E. J. W. List-Kratochvil, E. L. Unger, *Energy Technol.* **2020**, *8*, 1900991.
- [23] H. Eggers, F. Schackmar, T. Abzieher, Q. Sun, U. Lemmer, Y. Vaynzof, B. S. Richards, G. Hernandez-Sosa, U. W. Paetzold, *Adv. Energy Mater.* **2020**, *10*, 1903184.
- [24] J. E. Bishop, C. D. Read, J. A. Smith, T. J. Routledge, D. G. Lidzey, *Sci. Rep.* **2020**, *10*, 6610.
- [25] T. S. Le, D. Saranin, P. Gostishchev, I. Ermanova, T. Komaricheva, L. Luchnikov, D. Muratov, A. Uvarov, E. Vyacheslavova, I. Mukhin, S. Didenko, D. Kuznetsov, A. Di Carlo, *Sol. RRL* **2021**, *6*, 2100807.
- [26] C. Li, J. Yin, R. Chen, X. Lv, X. Feng, Y. Wu, J. Cao, *J. Am. Chem. Soc.* **2019**, *141*, 6345.
- [27] Y. Wu, D. Yan, J. Peng, T. Duong, Y. Wan, S. P. Phang, H. Shen, N. Wu, C. Barugkin, X. Fu, S. Surve, D. Grant, D. Walter, T. P. White, K. R. Catchpole, K. J. Weber, *Energy Environ. Sci.* **2017**, *10*, 2472.
- [28] Y. Wu, P. Zheng, J. Peng, M. Xu, Y. Chen, S. Surve, T. Lu, A. D. Bui, N. Li, W. Liang, L. Duan, B. Li, H. Shen, T. Duong, J. Yang, X. Zhang, Y. Liu, H. Jin, Q. Chen, T. White, K. Catchpole, H. Zhou, K. Weber, *Adv. Energy Mater.* **2022**, *12*, 2200821.
- [29] S. Moghadamzadeh, I. M. Hossain, T. Duong, S. Gharibzadeh, T. Abzieher, H. Pham, H. Hu, P. Fassel, U. Lemmer, B. A. Nejand, U. W. Paetzold, *J. Mater. Chem. A* **2020**, *8*, 24608.
- [30] H. Hu, S. Moghadamzadeh, R. Azmi, Y. Li, M. Kaiser, J. C. Fischer, Q. Jin, J. Maibach, I. M. Hossain, U. W. Paetzold, B. Abdollahi Nejand, *Adv. Funct. Mater.* **2022**, *32*, 2107650.
- [31] B. Abdollahi Nejand, D. B. Ritzer, H. Hu, F. Schackmar, S. Moghadamzadeh, T. Feeney, R. Singh, F. Laufer, R. Schmagier, R. Azmi, M. Kaiser, T. Abzieher, S. Gharibzadeh, E. Ahlswede, U. Lemmer, B. S. Richards, U. W. Paetzold, *Nat. Energy* **2022**, *7*, 620.
- [32] V. K. LaMer, R. H. T. Dinegar, *J. Am. Chem. Soc.* **1950**, *72*, 4847.
- [33] Y.-H. Seo, J. H. Kim, D.-H. Kim, H.-S. Chung, S.-I. I. n. Na, *Nano Energy* **2020**, *77*, 105164.
- [34] C. Zhang, J. F. S. Fernando, K. L. Firestein, J. E. von Treifeldt, D. P. Siriwardena, X. Fang, D. V. Golberg, *Appl. Mater. Today* **2020**, *20*, 100788.
- [35] M.-C. Tang, Y. Fan, D. Barrit, R. Li, H. X. Dang, S. Zhang, T. J. Magnanelli, N. V. Nguyen, E. J. Heilweil, C. A. Hacker, D.-M. Smilgies, K. Zhao, A. Amassian, T. D. Anthopoulos, *Sol. RRL* **2020**, *4*, 2000272.
- [36] J. M. Hoffman, J. Strzalka, N. C. Flanders, I. Hadar, S. A. Cuthriell, Q. Zhang, R. D. Schaller, W. R. Dichtel, L. X. Chen, M. G. Kanatzidis, *Adv. Mater.* **2020**, *32*, 2002812.
- [37] S. Lee, M.-C. Tang, R. Munir, D. Barrit, Y.-J. Kim, R. Kang, J.-M. Yun, D.-M. Smilgies, A. Amassian, D.-Y. I. n. Kim, *J. Mater. Chem. A* **2020**, *8*, 7695.
- [38] M. Qin, K. Tse, T. K. Lau, Y. Li, C. J. Su, G. Yang, J. Chen, J. Zhu, U. S. Jeng, G. Li, H. Chen, X. Lu, *Adv. Mater.* **2019**, *31*, 1901284.
- [39] M. Qin, P. F. Chan, X. Lu, *Adv. Mater.* **2021**, *33*, 2105290.
- [40] T. Trupke, B. Mitchell, J. W. Weber, W. McMillan, R. A. Bardos, R. Kroeze, *Energy Procedia* **2012**, *15*, 135.
- [41] J. Zikulnig, W. Mühleisen, P. J. Bolt, M. Simor, M. De Biasio, *Solar* **2022**, *2*, 1.
- [42] M. Liao, B. Shan, M. I. n. Li, *J. Phys. Chem. Lett.* **2019**, *10*, 1217.
- [43] S. Toda, E. W.-G. Diao, S. Shigeto, *J. Phys. Chem. C* **2021**, *125*, 27996.
- [44] M.-R. Ahmadian-Yazdi, M. Eslamian, *Langmuir* **2021**, *37*, 2596.
- [45] K. Schötz, F. Panzer, *J. Phys. Chem. A* **2021**, *125*, 2209.
- [46] F. Babbe, C. M. Sutter-Fella, *Adv. Energy Mater.* **2020**, *10*, 1903587.
- [47] Y. Sun, X. Wang, H.-Y. Y. Wang, S. Yuan, Y. Wang, X.-C. C. Ai, J.-P. P. Zhang, *J. Phys. Chem. Lett.* **2021**, *12*, 5357.
- [48] P. W. Fong, H. Hu, Z. Ren, K. Liu, L. Cui, T. Bi, Q. Liang, Z. Wu, J. Hao, G. Li, *Adv. Sci.* **2021**, *8*, 2003359.
- [49] A. Merdasa, C. Rehermann, K. Hirslandt, J. Li, O. Maus, F. Mathies, T. Unold, J. Dagar, R. Munir, E. Unger, *Res Sq* **2020**, <https://doi.org/10.21203/rs.3.rs-102041/v1>.
- [50] F. Mathies, E. R. Nandayapa, G. Paramasivam, M. F. Al Rayes, V. R. F. F. Schröder, C. Rehermann, E. J. W. W. List-Kratochvil, E. L. Unger, *Mater. Adv.* **2021**, *2*, 5365.
- [51] S. Ternes, F. Laufer, P. Scharfer, W. Schabel, B. S. Richards, I. A. Howard, U. W. Paetzold, *Sol. RRL* **2021**, *6*, 2100353.
- [52] F. Schackmar, H. Eggers, M. Frericks, B. S. Richards, U. Lemmer, G. Hernandez-Sosa, U. W. Paetzold, *Adv. Mater. Technol.* **2021**, *6*, 2000271.
- [53] J. J. van Franeker, K. H. Hendriks, B. J. Bruijnaers, M. W. G. M. Verhoeven, M. M. Wienk, R. a. J. Janssen, *Adv. Energy Mater.* **2017**, *7*, 1601822.
- [54] O. Rubel, S. D. Baranovskii, K. Hantke, B. Kunert, W. W. Rühle, P. Thomas, K. Volz, W. Stolz, *Phys. Rev. B* **2006**, *73*, 233201.
- [55] J. Li, X. Yuan, P. Jing, J. Li, M. Wei, J. Hua, J. Zhao, L. Tian, *RSC Adv.* **2016**, *6*, 78311.
- [56] B. Chen, J. Peng, H. Shen, T. Duong, D. Walter, S. Johnston, M. M. Al-Jassim, K. J. Weber, T. P. White, K. R. Catchpole, D. Macdonald, H. T. Nguyen, *Adv. Energy Mater.* **2019**, *9*, 1802790.
- [57] P. Gratia, I. Zimmermann, P. Schouwink, J.-H. Yum, J.-N. Audinot, K. Sivula, T. Wirtz, M. K. Nazeeruddin, *ACS Energy Lett.* **2017**, *2*, 2686.
- [58] K. Zhang, Z. Wang, G. Wang, J. Wang, Y. Li, W. Qian, S. Zheng, S. Xiao, S. Yang, *Nat. Commun.* **2020**, *11*, 1006.
- [59] W. Xiang, J. Zhang, S. (Frank) Liu, S. Albrecht, A. Hagfeldt, Z. Wang, *Joule* **2022**, *6*, 315.
- [60] A. S. Tutantsev, N. N. Udalova, S. A. Fateev, A. A. Petrov, W. Chengyuan, E. G. Maksimov, E. A. Goodilin, A. B. Tarasov, *J. Phys. Chem. C* **2020**, *124*, 11117.
- [61] N. K. Noel, S. N. Habisreutinger, B. Wenger, M. T. Klug, M. T. Hörantner, M. B. Johnston, R. J. Nicholas, D. T. Moore, H. J. Snaith, *Energy Environ. Sci.* **2017**, *10*, 145.

- [62] C. Wu, K. Wang, J. Li, Z. Liang, J. Li, W. Li, L. Zhao, B. Chi, S. V. Wang, *Matter* **2021**, 4, 775.
- [63] K. L. Gardner, J. G. Tait, T. Merckx, W. Qiu, U. W. Paetzold, L. Kootstra, M. Jaysankar, R. Gehlhaar, D. Cheyins, P. Heremans, J. Poortmans, *Adv. Energy Mater.* **2016**, 6, 1600386.
- [64] A. A. Petrov, A. A. Ordinartsev, S. A. Fateev, E. A. Goodilin, A. B. Tarasov, *Molecules* **2021**, 26, 7541.
- [65] Y. Deng, C. H. Van Brackle, X. Dai, J. Zhao, B. Chen, J. Huang, *Sci. Adv.* **2019**, 5, eaax7537.
- [66] J. C. Hamill, J. Schwartz, Y.-L. Loo, *ACS Energy Lett.* **2018**, 3, 92.
- [67] S. Chen, X. Dai, S. Xu, H. Jiao, L. Zhao, J. Huang, *Science* **2021**, 373, 902.
- [68] S. Ternes, J. Mohacsi, N. Lüdtkke, H. M. Pham, M. Arslan, P. Scharfer, W. Schabel, B. S. Richards, U. W. Paetzold, *ACS Appl. Mater. Interfaces* **2022**, 14, 11300.
- [69] F. Mathies, T. Abzieher, A. Hochstuhl, K. Glaser, A. Colsmann, U. W. Paetzold, G. Hernandez-Sosa, U. Lemmer, A. Quintilla, *J. Mater. Chem. A* **2016**, 4, 19207.
- [70] R. Massoudi, A. D. King, *J. Phys. Chem.* **1974**, 78, 2262.
- [71] M. V. Berry, *Phys. Educ.* **1971**, 6, 001.
- [72] E. J. Slowinski, E. E. Gates, C. E. Waring, *J. Phys. Chem.* **1957**, 61, 808.
- [73] Y. Jo, K. S. Oh, M. Kim, K. H. Kim, H. Lee, C. W. Lee, D. S. Kim, *Adv. Mater. Interfaces* **2016**, 3, 1500768.
- [74] W. S. Yang, J. H. Noh, N. J. Jeon, Y. C. Kim, S. Ryu, J. Seo, S. I. Seok, *Science* **2015**, 348, 1234.
- [75] Z. Li, M. Yang, J.-S. S. Park, S.-H. H. Wei, J. J. Berry, K. Zhu, *Chem. Mater.* **2016**, 28, 284.
- [76] J.-W. Lee, D.-H. Kim, H.-S. Kim, S.-W. Seo, S. M. Cho, N.-G. Park, *Adv. Energy Mater.* **2015**, 5, 1501310.
- [77] S. Gharibzadeh, P. Fassel, I. M. Hossain, P. Rohrbeck, M. Frericks, M. Schmidt, T. Duong, M. R. Khan, T. Abzieher, B. A. Nejand, F. Schackmar, O. Almora, T. Feeney, R. Singh, D. Fuchs, U. Lemmer, J. P. Hofmann, S. A. L. Weber, U. W. Paetzold, *Energy Environ. Sci.* **2021**, 14, 5875.
- [78] A. Farag, R. Schmagel, P. Fassel, P. Noack, B. Wattenberg, T. Dippell, U. W. Paetzold, *ACS Appl. Energy Mater.* **2022**, 5, 6700.
- [79] A. Al-Ashouri, A. Magomedov, M. Roß, M. Jošt, M. Talaikis, G. Chistiakova, T. Bertram, J. A. Márquez, E. Köhnen, E. Kasparavičius, S. Levenco, L. Gil-Escrig, C. J. Hages, R. Schlatmann, B. Rech, T. Malinauskas, T. Unold, C. A. Kaufmann, L. Korte, G. Niaura, V. Getautis, S. Albrecht, *Energy Environ. Sci.* **2019**, 12, 3356.